Mechanism and Machine Theory 197 (2024) 105647

Contents lists available at ScienceDirect

Mechanism and Machine Theory

journal homepage: www.elsevier.com/locate/mechmt

Research paper

Modeling of flexible shaft for robotics applications[☆]

Muhammad Usman [a,c,*], Amin Khorasani [a,b], Thierry Hubert [a,b], Raphaël Furnémont [a,b], Bram Vanderborght [a,c], Dirk Lefeber [a,b], Greet Van de Perre [a,c], Tom Verstraten [a,b]

[a] *Brubotics, Vrije Universiteit Brussel, Brussels, Belgium*
[b] *Flanders Make, Brussel, Belgium*
[c] *Imec, Brussels, Belgium*

ARTICLE INFO

Keywords:
Actuator design
Compliant actuators
Actuator modeling

ABSTRACT

Reducing moving mass and effective inertia is essential for achieving safe human–robot collaboration. This can be achieved either by employing remote actuation, which moves the mass of actuators away from the moving elements of the robot, or by elastic actuation, which decouples the inertia of the actuator from the inertia of the robot's link. Flexible shafts, being torsionally compliant slender long shafts, offer a combination of remote and series elastic actuation over an obstacle. Modeling such transmission is complicated due to its three-dimensional deformation in torsion, bending, and helical buckling. This paper proposes an algorithm for estimating the polar moment of inertia and stiffness of the flexible shafts using their physical dimensions of length and diameter. Using an inertia-spring–damper model, the stiffness parameters are estimated experimentally for nine flexible shafts with variable diameters and lengths in straight and bent configurations. The proposed algorithm is validated with experimental stiffness values for variable diameters and lengths in straight configuration. For bent configuration, an empirical formulation is provided to incorporate the bending deformation effect till a bending angle of 45°.

Elasticity and remote actuation based on tendons/cables/belts systems are crucial for enhancing human–robot interaction. They are widely utilized in safe robotic applications such as wearable and collaborative robots, providing compliance, reduced mass, and flexibility. Series elastic actuators, in particular, have been extensively applied in robotics, offering a safer and more energy-efficient interaction with the environment, thanks to their built-in spring element [1]. Research has extensively explored the design, modeling, and control of series elastic actuation, underlining its significance across various robotic applications [2,3]. Verstraten et al. [4,5] have specifically examined the optimal design of elastic actuation in general robot applications and powered ankle-foot prostheses.

In the domain of remote actuation, tendon-driven actuation has been widely adopted to reduce moving mass and inertia in robots. Cable-driven mechanisms have been developed for robot arms, showcasing benefits such as low moving mass and enhanced dexterity [6,7]. Wearable robots have also integrated cable-driven transmission systems for their compactness and back-drivability advantages [8]. Due to offered compliance and structural compactness of cable-driven actuation systems, it found its application in modern-day manipulators in the form of continuum and tensegrity robots [9,10].

Additionally, remote actuation based on tendons/bowden cable systems and series elasticity concepts have been employed together to harness their respective advantages for human–robot collaboration [11,12]. Grosu et al. [13] used a tendon-driven actuation technique for a powered orthosis. A low-cost seven-degree-of-freedom robot [14], was developed employing series elasticity and cable actuation for achieving low mass and human safety. Though this combination of elastic and remote actuation

---

[☆] This research is supported by Research Foundation Flanders, Belgium (FWO) SBO project ELYSA Project (grant number S001821N) and grants 12Z7920N and 1505820N.

[*] Correspondence to: Pleinlaan 2, Building Z, 1050 Brussels, Belgium.
E-mail address: muusman@vub.ac.be (M. Usman).

https://doi.org/10.1016/j.mechmachtheory.2024.105647
Received 14 November 2023; Received in revised form 3 April 2024; Accepted 5 April 2024

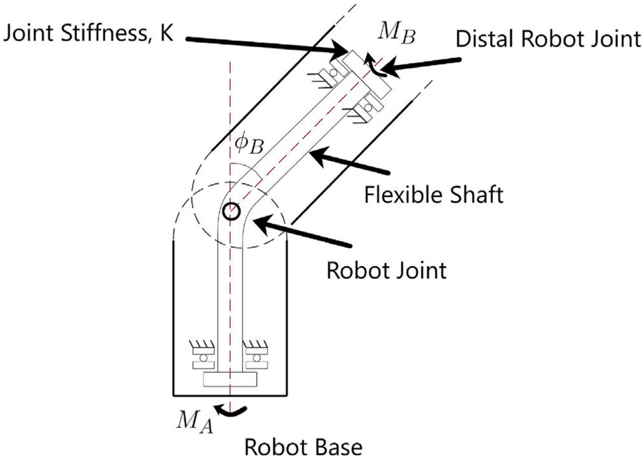

Fig. 1. Robot's configuration with flexible shaft actuation.

offers mechanical advantages for modern robotics, there lies an added complexity concerning such robots' design, modeling, and control. Different possible configurations of series elastic actuation offer different modeling and behavior [3,4]. Vallery et al. [15] discusses the accurate control of series elastic actuators. Similarly, remote actuation with tendons results in non-collocation, complicating the control of the robot [16]. Accurate dynamic models have been developed to further enhance their implementation, addressing the issues of slack and sliding friction [17,18]. With each actuation concept being sophisticated in their control, combining them offers additional control challenges along with their mechanical complexity.

Rodriguez-Cianca et al. [19] introduced a novel remote torsional actuator using a flexible shaft for wearable robots, which possesses the inherent qualities of series elastic and remote actuation. In its mechanical simplicity and light-weight nature, this compliant element holds a strong potential for applications where the reduction of moving mass is essential and elastic joints are required. Robot arms for Human–Robot Interaction require elastic joints and low inertia links [20]. As such, the flexible shaft-based transmission offers a single-step combined solution for introducing elasticity in robot joints and reducing robot inertia.

Owing to its combined advantages of elasticity and remote actuation, it has found different applications in robotics, such as a surgical robotic manipulator [21], a novel soft actuator [22] and a search robot actuated by flexible shafts [23]. Flexible shafts have also been used as compliant remote actuation in medical applications like endoscopy, colonoscopy, and surgical robot tool [24]. Flexible shafts also found their application in human assistance devices, where a flexible shaft is utilized to transmit torque remotely from the waist to ankle [25,26] and trunk [27].

Tan et al. [22] developed a novel soft-actuator based on flexible shafts, capable of push-pull and twist using the shafts' compliant characteristics. The work models a flexible shaft using beam theory for torsion, considering the cross-section as a circle. Liu et al. [28] developed a soft gripper actuated using a single flexible shaft for a finger, making it bend and rotate to achieve dexterous object manipulation. The work utilizes the flexible shaft's empirical formulation for its control. An empirical model was also proposed in [19], where a single flexible shaft's input–output characteristics have been modeled using the Fourier-Series approximation technique. The proposed model, though accurate, needs more insight into the physical characteristics of a flexible shaft, which is essential for designing an actuator for a specific robot application.

A miniaturized version of the drill string is developed using a flexible shaft and drill bit performing drilling operations on small-size rocks in lab settings [29]. The research study develops finite element modeling of flexible shafts as a solid cylinder, supported by experimental identification of stiffness parameters to achieve an accurate model adjustment with respect to the experiments. The model lacks the modeling of intrinsic characteristics based on the flexible shaft's construction. Moreover, the application of an oil rig works in the rotation of a flexible shaft in a straight or pre-defined bent configuration, which limits its correlation to robotic application, where bidirectional torsion and continuous bending are involved.

A flexible shaft as a tightly wounded wire coil, forming layers on top of each other in opposite directions, requires a model based on its construction and geometry parameters. Thus, a thorough physics-based modeling of this transmission is required, which can make understanding this hybrid remote and elastic element easier and expand its utility in robotic applications. Modeling the behavior of this remote and torsionally compliant actuator is challenging. Due to its long, slender shaft construction, the flexible shaft can deform three-dimensionally, namely, torsion, bending, and helical buckling. With the increase in length and decrease in the diameter of a flexible shaft, its physical characteristics change from nearly a rigid shaft to nearly a torsional spring. An extensive study of flexible shafts with variable diameters and lengths is required to encompass this resemblance in behavior.

This paper focuses on the physics-based modeling of flexible shafts as remote torsional and compliant actuation for transmitting torque over obstacles such as robot joints, as shown in Fig. 1 to achieve desired joint stiffness and lightweight transmission. Nine flexible shafts are selected, with five flexible shafts having variable diameters and fixed lengths and four flexible shafts with fixed diameters and variable lengths. An algorithm to estimate the parameters of the polar moment of inertia and stiffness is proposed

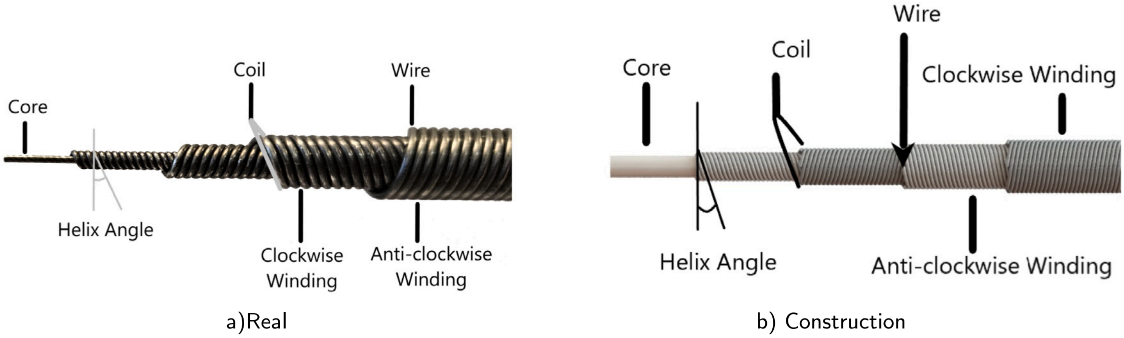

Fig. 2. Flexible shaft.

based on the physical dimensions of the flexible shafts. Using a second-order system based on the torsional mass–spring–damper model, the experimental input–output characteristics of flexible shafts with the change in length, diameter, and bending angle are analyzed. Experimental results show the stiffness parameters using curve-fitting, highlighting the minimal contribution of inertia and damping parameters. The experimental stiffness parameters are finally compared with geometrically estimated stiffness parameters for validation. Due to the complexity and computational cost of lumped parameter modeling and finite element modeling, this work does not consider other modeling techniques for brevity.

The paper is organized as follows: Section 1 discusses the modeling of flexible shafts, starting with their construction and physical analogy to torsional springs and rigid shafts. It describes the theoretical estimation method of the physical parameters of flexible shafts using geometry. A model for the flexible shaft is introduced based on the inertial-spring–damper model. Section 2 describes the experimental setup and procedure. It further discusses the experimental results of flexible shafts as the input–output characteristics in a straight and bent configuration. Section 3 discusses the evaluation of the inertial-spring–damper model in straight and bent configurations, followed by the evaluation of the geometrical model with the experimental results. Sections 4 and 5 discuss the results and conclude the paper by outlining the future objectives of this research.

1. Modeling of flexible shaft

Fig. 2 shows real and construction schematics of a flexible shaft. A set of wires forms a tightly wounded coil on top of another coil. The winding direction of adjacent coils is kept opposite to each other. The core is made usually with a single strand, as shown in Fig. 2. Alternatively, it is also made as a set of wires with a high helix angle. The helix angle at which the winding of wires is performed is critical for their tensile and torsional strength. The helix angle, with respect to a cross-sectional plane of the shaft, is kept high to attain high tensile strength. Conversely, a smaller helix angle is used to attain torsional strength. Furthermore, to avoid the rotation or to untwist these coils, the direction of winding is inverted so that the adjacent layers of coils counteract each other's unwinding on the application of external torque. Flexible shafts from manufacturers come with end fittings for connection with a motor and load. Fig. 2(a) shows a flexible shaft cut opened at one end by removing the end fitting. Here, the number of wires in a coil, the diameter of the coil wire, and the diameter of the core define the rated torque and stiffness (both torsional and bending) of the flexible shaft. Only one flexible shaft is cut open, and others are not for validation purposes.

Due to its construction as tightly wounded layers of wire coils, a flexible shaft has a physical analogy with torsional springs and rigid shafts. The following subsection discusses this analogy.

1.1. *Flexible shaft as a torsional spring*

A torsional spring, a tightly wounded coil, resembles a single layer of a flexible shaft in its characteristics. A flexible shaft can thus be seen as a set of parallel torsional springs nested inside each other in an anti-clockwise and clockwise direction. For any torsional spring, the stiffness or spring constant K per turn is given by:

$$K = \frac{\tau}{\theta} = \frac{Ed^4}{10.2DN} \tag{1}$$

Here, E is Young's modulus, d is the diameter of the wire, D is the diameter of the coil or spring, and N is the effective number of turns in the spring coil. The relationship of the diameter of wire d and D with the stiffness is interesting for flexible shafts as their respective change alters their stiffness bounded by the spring index $C = \frac{D}{d}$ for feasible spring's dimensions.

Once a torque is applied to a torsional spring opposite the winding direction, it increases the diameter of the coil and reduces its length [30]. For a torque applied in the winding direction, the diameter decreases, and the length increases. This conservation of volume is restrained in the case of a flexible shaft, causing it to apply stresses on the adjacent layers, making it a multi-layer restrained torsional spring. Once torque is applied in the opposite direction of winding for the outermost coil of a flexible shaft, the outermost layer pushes to unwind. The contribution of the outermost layer towards the torsional characteristics can be formulated as a helical torsional spring with equivalent wire and helix diameters using (1).

Conversely, the outermost layer tightly packs the inner layers under the torque application in the winding direction. This results in asymmetrical torsional stiffness of a flexible shaft due to the torsional spring-like nature of the outermost layer. This can be related to layer jamming mechanisms where stiffness changes with the change in stresses between layers by controlling vacuum pressure levels [31].

1.2. Flexible shaft as a rigid shaft

Though rigid shaft composition is continuous and dissimilar to that of the flexible shaft, the calculation of the parameters of a rigid shaft can be analogous in principle to it due to the tightly packed nature of coils on top of each other resembling a jamming mechanism scenario [31]. The rotational inertia J, polar moment of inertia, J_p, and stiffness K of a rigid shaft with mass m, outer diameter D, and length L are given as:

$$J = \frac{m}{8} D^2 = \rho L J_p, \quad J_p = \frac{\pi}{32} D^4 \tag{2}$$

$$K = J_p \frac{G}{L} \tag{3}$$

Here, ρ is the density, and G is the shear modulus of the rigid shaft's material.

Due to the tightly packed nature of adjacent coils in a flexible shaft with nearly a rigid core, its behavior resembles a rigid shaft. With the increase in the flexible shaft's diameter and decrease in length, it nearly behaves like a rigid shaft with little bending compliance. The analogy of a flexible shaft as a rigid shaft is vital to estimate the moment of inertia and stiffness parameters with geometric modification to (2) and (3).

1.3. Theoretical estimation of physical parameters

In the case of the flexible shaft, the geometry of the cross-section is different from a rigid shaft, as shown in Fig. 3. Recalling the construction of the flexible shaft as shown in Fig. 2, the core wires of a flexible shaft make a high helix angle with the plane of its cross-section, and coil wires make a small helix angle. Being at a high helix angle for the wires of a flexible shaft core, the cross-section of core wires is circular due to their center line being nearly orthogonal to the plane of the cross-section of a flexible shaft. On the other hand, due to the small helix angle of the coil wires with the cross-section plane of the flexible shaft, the wires contribute to the cross-section area as an ellipse shape approximately instead of a circle shape, as shown in Fig. 3. This results in a series of ellipse shapes in a circular path at a distance from the centerline of a flexible shaft equal to the radius of the coil. This repeats for all the coil layers of a flexible shaft and can be seen in Fig. 3. This creates a geometry different from a rigid shaft with hollow spaces between ellipses and requires alternative treatment to estimate inertia and stiffness parameters accurately. Therefore, the cross-section of a flexible shaft is divided into two sections, core (black outlined) and coil layers (red outlined as a single coil layer), as highlighted in Fig. 3(a). The core can be identified as a rigid shaft with a circular cross-section at the center line of a flexible shaft. The coil layers section, however, requires a segregated layer treatment. Thus, the moment of inertia J of the flexible shaft with N_{coils} combining two sections of core and coils is given by:

$$J = \rho L (J_{core} + \sum_{i=1}^{N_{coils}} J_{coil}[i]) \tag{4}$$

where, N_{coils} for a flexible shaft with diameter, D, its core diameter, D_{core} and wire diameter, d_{wire} of a coil, is given by:

$$N_{coils} = \frac{D - D_{core}}{2 * d_{wire}} \tag{5}$$

For the coil layers, the wire's polar moment of inertia is approximated as an ellipse located at a distance R_{coil} from its center to the center line of the flexible shaft as shown in Fig. 3. Using the parallel axis theorem and formula of polar moment of inertia for an ellipse, the polar moment of inertia J_{wire} for a single wire of a coil layer is given by:

$$J_{wire} = \frac{\pi}{4}(a^3 b + b^3 a) + \pi a b R_{coil}^2 \tag{6}$$

Here, a is the major radius, and b is the minor radius of an ellipse, see Fig. 3.

Thus, for the case of N_{wires} wires in an ith coil layer, the J_{coil} polar moment of inertia for a coil layer is given by:

$$J_{coil}[i] = N_{wires}[i] \left(\frac{\pi}{4}(a_i^3 b_i + b_i^3 a_i) + \pi a_i b_i R_{coil}[i]^2 \right) \tag{7}$$

where, the major, a, and minor radius, b, can be calculated as:

$$a_i = \frac{\pi R_{coil}[i]}{N_{wires}[i]}, \quad b_i = \frac{d_{wire}[i]}{2}$$

The polar moment of inertia in Eq. (7) has to be repeatedly calculated for other coil layers, which is used in the summation mentioned in Eq. (4) to find the total polar moment of inertia of a flexible shaft.

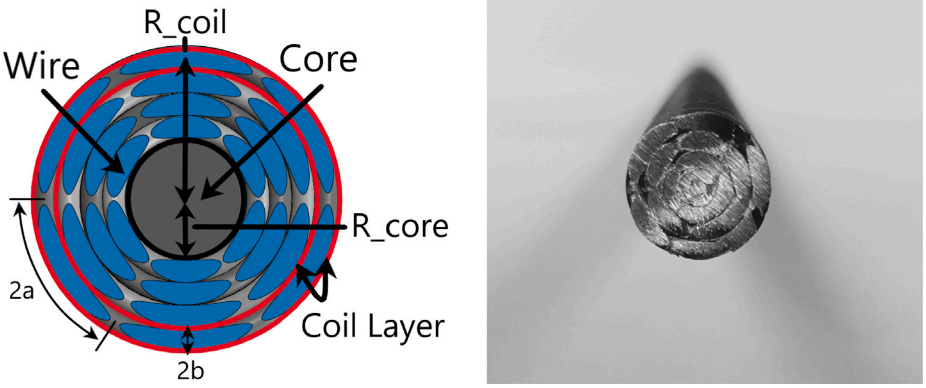

a) Schematics

b) Real

Fig. 3. Cross section view of flexible shaft. (For interpretation of the references to color in this figure legend, the reader is referred to the web version of this article.)

Using Eq. (3), the stiffness of the flexible shaft for both directions is given by:

$$K_p = (J_{core} + \sum_{i=1}^{N_{coils}} J_{coil}[i])\frac{G}{L} \tag{8}$$

$$K_n = (J_{core} + \sum_{i=1}^{N_{coils}-1} J_{coil}[i])\frac{G}{L} \tag{9}$$

Density ρ and Shear Modulus, G of Spring Steel Wire ASTM A228, are considered for the calculations. The values used are $7.8e{+}3\ \mathrm{kg/m^3}$ and $7.0e{+}10$ Pa, respectively. Outermost coil is ignored for the opposite direction of winding's stiffness due to its negligible contribution acting as a torsional spring of equivalent helix diameter, D and wire diameter, d, as given by Eq. (1).

Thus, the theoretical values of inertia and stiffness can be calculated as given by the Eqs. (4) and (8) provided the values of a flexible shaft's length L, coil radius, R_{coil} of all winding layers, number of wires in a coil layer, N_{wires} and diameter of wire $d_{wire} = 2b_i$ used in each coil layer is known.

Algorithm 1 Estimation of Parameters of a Flexible shaft.

```
$D_{core} \leftarrow D/5$
$N_{coils} \leftarrow \frac{D-D_{core}}{2*d_{wire}}$
$\delta \leftarrow N_{coils} - round(N_{coils})$
if $\delta > 0$ then
    $D_{core} = D_{core} + 2 * \delta * d_{wire}$
else
    $D_{core} = D_{core} - 2 * \delta * d_{wire}$
end if
$N_{coils} \leftarrow round(N_{coils})$
$l \leftarrow \frac{d_{wire}}{cos\alpha}$
$i = 1$
while $i \le N_{coils}$ do
    $D_{coil}[i] \leftarrow d_{wire} + 2 * d_{wire} * (i-1) + D_{core}$
    $L_h[i] \leftarrow \pi D_{coil}[i]\ tan\alpha$
    $N_{wires}[i] \leftarrow \frac{L_h[i]}{l}$
    $i{+}{+}$
end while
```

Flexible shaft manufacturers provide no information regarding these parameters. Manufacturers produce the shafts with heat treatment at their ends to fuse the coils to avoid untwisting/uncoiling. Afterward, the process of swaging attaches end fittings of the customer's choice for coupling it with a motor and a load. Therefore, finding these physical parameters for each flexible shaft becomes nearly cumbersome or infeasible as it will involve cutting the shafts. For modeling, a spare flexible shaft is cut and opened as shown in Fig. 3, on its end fittings to measure the values required for calculating physical parameters. The measurements of flexible shaft's diameter and wire diameters are made using vernier caliper and screw gauge with the resolutions of 0.01 mm and

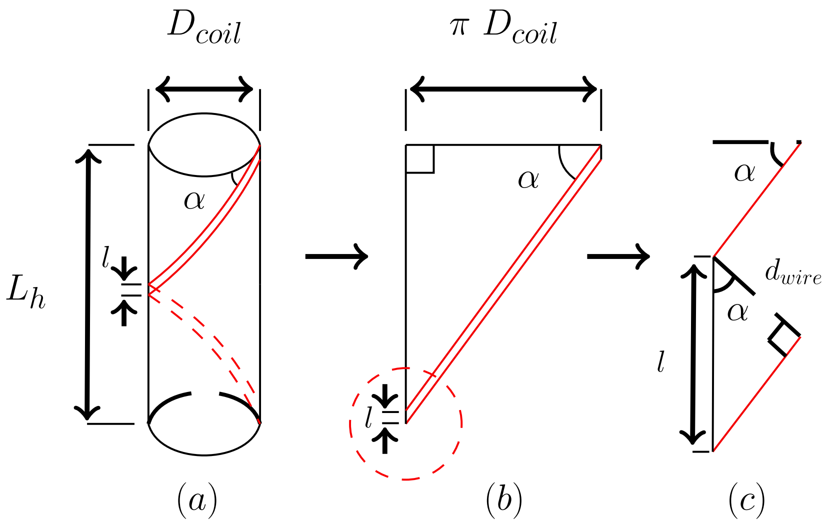

Fig. 4. One helix turn of a coil wire. (For interpretation of the references to color in this figure legend, the reader is referred to the web version of this article.)

0.001 mm respectively. Using the observations, the estimation of required parameters for stiffness and inertia calculation of a flexible shaft can be performed with the following guidelines:

- J_{core} in Eqs. (4) and (8) is estimated using the rigid shaft equation (2). The diameter, D_{core} for J_{core}, is estimated based on the observation made by the cross-section shown in Fig. 3, which is approximate $D_{core} = D/5$. Here, D is the diameter of a flexible shaft. Variation in the diameter of the core of a flexible shaft changes its torsional and bending stiffness like a rigid shaft.
- Only the flexible portion, excluding the length of the end fittings, is measured for the length, L, of a flexible shaft.
- The diameter of a coil wire, d_{wire} in the outermost coil layer, can be measured easily from the surface. Using Eq. (5), the number of coil layers N_{coils} can be estimated. In the case of a fraction result for N_{coils}, the fraction part is added or subtracted to D_{core}.
- The Helix angle of the outermost coil layer can also be measured from the surface of a flexible shaft. For internal coils, the value of the helix angle is assumed to be the same as per observation, shown in Fig. 2(a). This information can lead to the number of wires, N_{wires} used in a coil layer by using trigonometry on one helix turn of a wire with its known diameter, d_{wire}, at a given helix angle, α, around a cylinder as demonstrated in Fig. 4. It makes a right-angle triangle with the helix angle, α as the angle opposite to the perpendicular, and the triangle's base as the cylinder's circumference. Fig. 4(a) shows a helix of a wire in red wrapped around a cylinder in one turn, (b) shows a right triangle unwrapped for the wire, and (c) shows a right triangle made by the wire at the corner of (b) triangle, showing it is a contribution to the pitch of one turn. Here, L_h is the pitch of the helix by wire, and l is the contribution of a wire in a pitch. One can find the number of wires in a coil layer by $\frac{L_h}{l}$. A usual value of $\pi/6$ is observed among the nine flexible shafts.
- Interval of D_{core} and d_{wire} is selected as $[\frac{D}{10}, \frac{D}{2}]$ and $[d_{wire} - 1e{-}4, d_{wire} + 1e{-}4]$ respectively to create maximum and minimum bounds for other possible construction of flexible shafts, providing a feasibility bound like a spring index C in torsional springs.

Using algorithm 1 and the above formulation, one can find the inertia and stiffness of a flexible shaft by measuring the length L and Diameter D of a flexible shaft, the diameter of outermost coil wire, d_{wire} and helix angle, α only.

1.4. Model as inertial spring–damper model

To model the behavior of the flexible shaft, an important consideration is to be made about its asymmetrical nature. Due to asymmetrical clockwise and anti-clockwise windings, its stiffness in both directions is nonidentical. When a torque is applied in one direction, the torsion causes the coils to either unwind or wind with respect to the direction of the torque, causing relaxing or stiffening of the outermost layer. In both cases, the stresses among the coil layers are different, and their effect is worth noticing.

A set of two torsional mass–spring–damper models [32] is considered to comprehend the asymmetrical behavior. The positive direction of the twist angle θ is defined as the direction of the outermost coil's winding of the flexible shaft. A separate set of stiffness and damping coefficients are considered for each direction. The stiffness parameters K_p and K_n, damping parameters B_p, and B_n are considered for positive and negative twist angle θ, respectively. Hence, the piece-wise function for torque τ is given as:

$$\tau = f(\theta) = \begin{cases} J\ddot{\theta} + B_n\dot{\theta} + K_n\theta & \theta < 0 \\ J\ddot{\theta} + B_p\dot{\theta} + K_p\theta & \theta \geq 0 \end{cases} \tag{10}$$

The inertia J is considered the same for both directions of input torque τ, since the cross-sectional geometry of the flexible shaft is the same for both directions of torque.

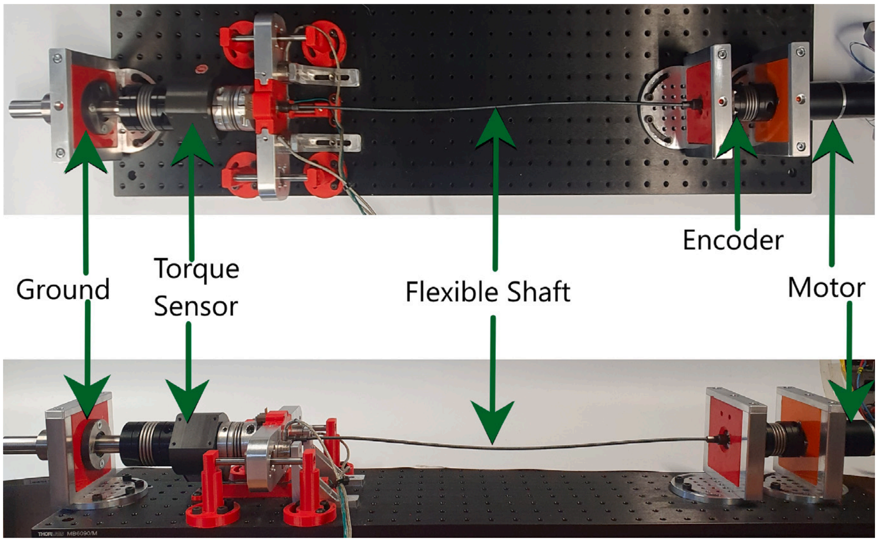

Fig. 5. Experimental setup.

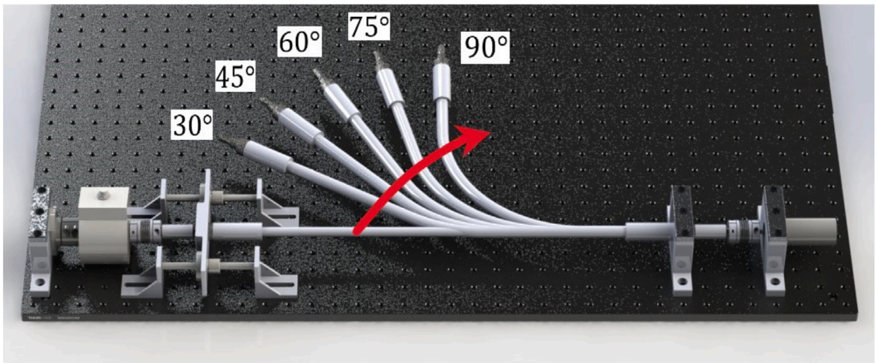

Fig. 6. Bending configuration — 0° to 90°.

2. Experiments

This section discusses the experimental setup, procedure and the results attained in straight and bending configuration for nine flexible shafts with different diameter and length.

2.1. Experimental setup and procedure

Fig. 5 shows the experimental setup used for the input–output characteristics of flexible shafts. A Maxon brushless DC motor (Catalog no. 167178) with a planetary gearbox (Gear ratio 91:1, catalog no. 203125) is used as a torque source. Flexible shafts Linkflex (without casings) from SSWhite Uk Ltd. are used with a diameter range of 4–12 mm and a length range of 235–535 mm. For benchmarking, nine flexible shafts with variable diameters and lengths are selected. The flexible shafts are selected to encompass the low to high stiffness range, with a possible bending angle of $\phi_B = 90°$. A DBRK-20 analog torque sensor (ETH-Messtechnik) with a measurement range of 20 N m is used for the torque measurement. The torque sensor is fixed at the load end, and its other end is connected with a flexible shaft's end fitting. An optical encoder EM2 from US Digital is used between the motor's output and the input of the flexible shaft to measure the twist angle θ of flexible shafts. For data acquisition, Beckhoff IO modules are used alongside the Maxon Driver EPOS3, integrated with TwinCAT EtherCAT.

All these components are connected through bellow shaft couplings to compensate for the rotation axis misalignment with no backlash. The ends of the flexible shaft are fixed for a linear motion to restrict any linear contraction due to helical buckling. 3-D

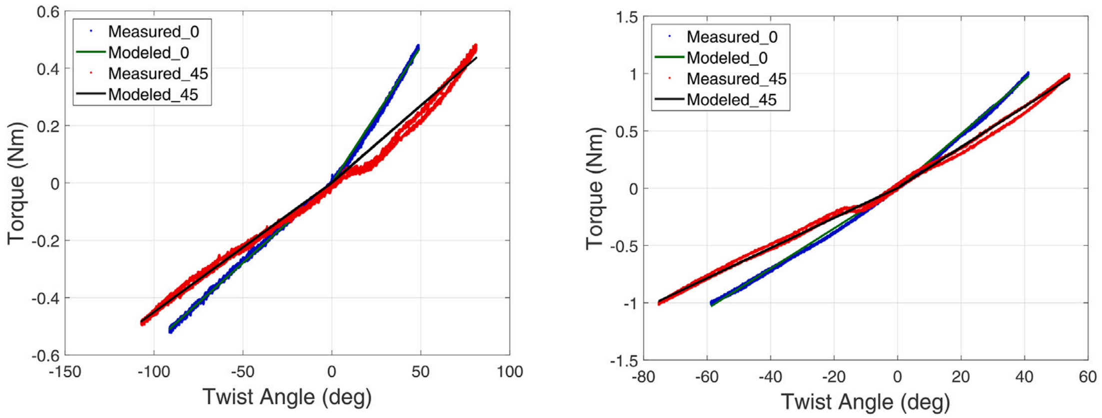

a) Flexible Shaft - D = 4 mm

b) Flexible Shaft - D = 5 mm

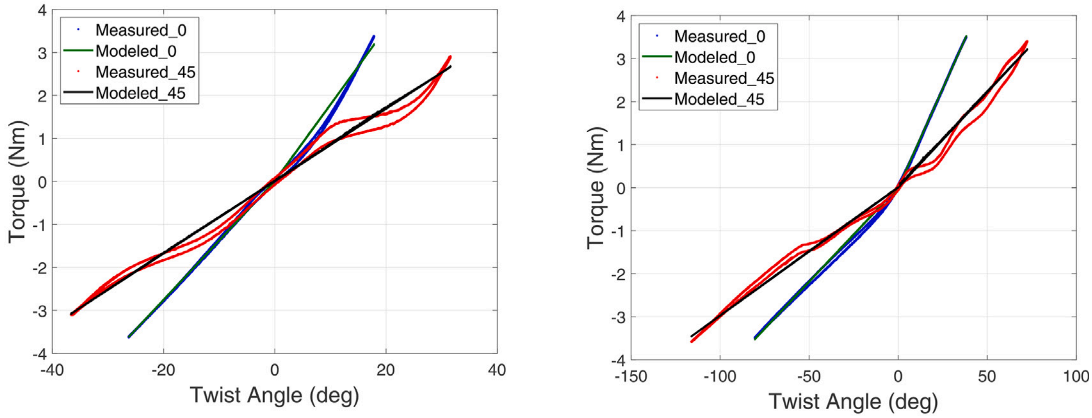

c) Flexible Shaft - D = 6 mm

d) Flexible Shaft - D = 8 mm

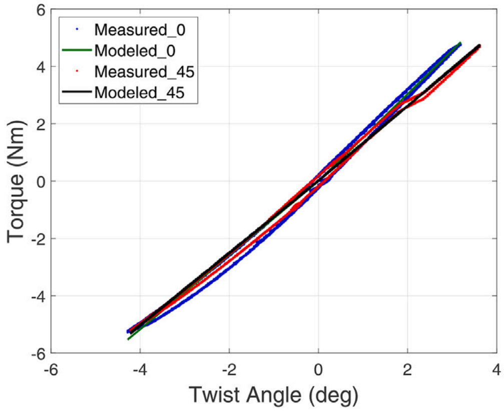

e) Flexible Shaft - D = 12 mm

Fig. 7. Input output characteristics at 0° and 45° bend angle.

printed generic brackets are used for both ends of the flexible shafts to install various flexible shafts easily. These brackets can be mounted in different positions on an optical breadboard to achieve different bending angles, as shown in Fig. 1.

An input chirp signal for desired torque τ for each flexible shaft is fed to the torque controller ranging from 0.5 to 20 Hz in frequency. The amplitude of desired torque signals is selected based on the nominal torque of each flexible shaft. The exact desired torque profile is followed for the bending angles of each flexible shaft varied from $\phi_B = 0°$ to $90°$ with 15° step in between as shown in Fig. 6. In the bending experiments, the flexible shaft is not supported along the length, so the intrinsic behavior can be observed without any reaction forces of supports. Implementation is done using MATLAB Simulink and TwinCAT shell for Microsoft Visual Studio using EtherCAT tutorial [33].

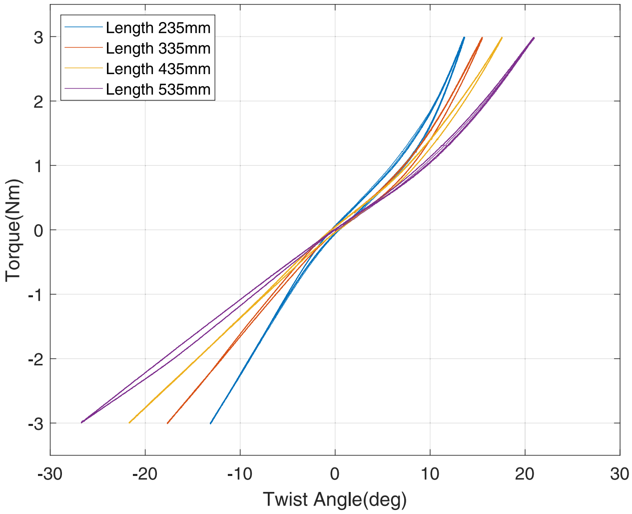

Fig. 8. Input output characteristics at $\phi_B = 0°$, D = 8 mm and varying L.

2.2. Experimental results

This section evaluates the relationship of the input twist angle θ with the output torque τ. The input–output characteristics of five flexible shafts with variable diameter and constant length are presented at straight and bending configurations of $\phi_B = 0°$ and 45° in Fig. 7. For bending angles 45° onwards, the results are shown for a single flexible shaft by Fig. 10.

2.2.1. Straight configuration

For the 0° bend angle shown in Fig. 7, the relation of applied torque τ and twist angle θ for the positive direction of torque show almost linear spring behavior with negligible hysteresis. For the negative side twist angle θ, the flexible shafts behave more closely like a linear spring. It can be observed that each direction of the twist angle possesses its non-identical behavior in terms of stiffness and hysteresis. This can be related to the winding and unwinding of the coil in the outermost coil layer. The negative twist angle θ is opposite to the direction of the outermost coil's winding, where the outermost layer unwinds. This unwinding causes the flexible shaft to lose stiffness as the outermost coil no longer applies stress to adjacent layers. For the positive twist angle θ, the outermost layer of coils winds and applies stress to the adjacent layers resulting in a stiffer, tight-wounded shaft. As seen in the input–output characteristics, the slope of the input–output characteristics graph for the positive twist angle side of the flexible shaft is higher than in comparison to the negative twist angle side.

With the increase in diameter of the flexible shafts, the input–output characteristics for both positive and negative twist angles stay similarly linear. However, the hysteresis increases in flexible shafts with a large diameter, as depicted in Fig. 7(c)(d)(e). As the diameter increases, the coil layers and their respective wire diameter also increases. As soon as a motor applies a torque, there are more stresses and friction in adjacent layers of flexible shafts. This increased energy loss generates a noticeable hysteresis region for thick flexible shafts.

The input–output characteristics for variable length and fixed diameter are attained at straight configuration to analyze the behavior of flexible shafts with different lengths. Fig. 8 shows the characteristic of four different flexible shafts with a change in length by a step of 100 mm. A decline in stiffness with the increase in length can be observed similar to the relationship proposed by Eqs. (3) and (8).

2.2.2. Bending configuration

In the bent configuration, the torsional stiffness of the flexible shaft declines as it is under stress at its inner and outer curvature. As the bending deformation is applied, the angle between the input and output axes increases, making transmitting torque over the bend difficult. Under this state, when a torque is applied, the deformation or twist angle θ due to torsion increases with the bending angle, ϕ_B. A higher bending angle, ϕ_B of 45° causes more twist angle θ for the same output torque τ, as shown in Fig. 7. It can be seen that the positive and negative sides of the input–output characteristics get more non-linear in comparison with the straight configuration in Fig. 7. Flexible shafts under bending stresses and compromised torsional stiffness can easily undergo helical buckling, as shown in Fig. 9. This phenomenon of helical buckling introduces non-linearity as there are regions of a nearly constant torque at the output with a twist angle θ being changed. When the buckling is being achieved, the shaft delivers almost constant output torque τ. This creates nearly horizontal steps in the torque-twist angle curve.

With the increase in diameter, the input–output characteristics of flexible shafts tend to go from non-linear behavior to linear behavior as shown in Fig. 7. For thin shafts, their helical buckling limit is lower than the thick shafts due to their low torsional and

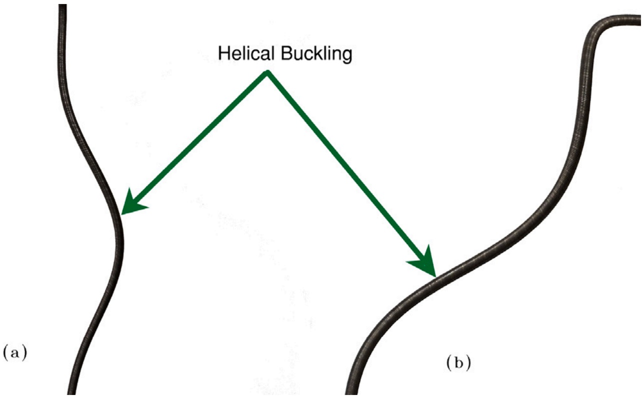

Fig. 9. Helical buckling at (a) 0° bend (b) 90° bend.

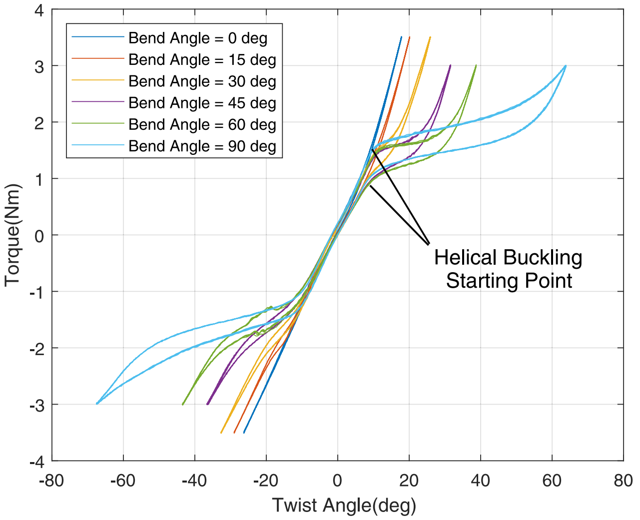

Fig. 10. Input-Output characteristics of 8 mm flexible shaft — $\phi_B = [0°, 90°]$.

bending stiffness. This explains the non-linearity introduced in a bent configuration. Fig. 10 depicts the input–output characteristics of a single shaft for higher bending angles where this phenomenon can be seen more clearly. Helical buckling occurs between 1.5 and 2 N m torque values (in the forward direction) or 1 and 1.5 N m (in the backward direction), regardless of bend angle. For higher bend angles the twist angle increases during buckling. These characteristics of helical buckling happen differently for each flexible shaft. For the case of a 12 mm flexible shaft, the torsional and bending stiffness is high enough to avoid buckling, as evident from Fig. 7.

Fig. 7(a) to (e) shows the slight increase in hysteresis with the increase in diameter for 45° bend angle, similar to what was observed in a straight configuration. However, it is more evident for the bent configuration than the straight configuration due to the additional stresses and friction due to helical buckling and bending. Fig. 10 further highlights this trend of increasing hysteresis with the bend angle of the flexible shaft.

To study the effect of dynamics on the input–output characteristics of a flexible, a chirp signal ranging from 0.5 Hz to 20 Hz is used for all the flexible shafts. A bode plot analysis is done for the thickest flexible shaft to demonstrate the impact of inertia of flexible shafts, as shown in Fig. 11. The plot shows a positive constant magnitude for frequencies up to 20 Hz. This demonstrates that the natural frequencies of flexible shafts used are high due to low inertia values. The bandwidth limit of the controller is achieved before reaching the resonant frequency of the flexible shafts. Since the inertia term has no impact on the torque for the specified range of frequencies, it can be inferred that a flexible shaft behaves purely like a spring for robotic systems where the requirements are high torque and slow speed in actuation units.

3. Model evaluation

This section discusses the model evaluation of Eq. (10). Moreover, the geometric model provided by Eqs. (8) and (9) using algorithm 1, is also discussed with experimental results.

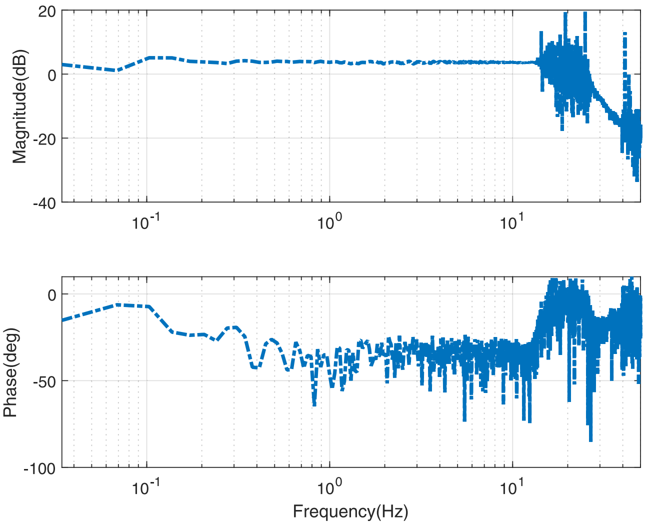

Fig. 11. Flexible shaft (Diameter 12 mm) - Bode plot - Bend angle 0°.

Table 1
Inertia torsional spring–damper model parameters — $\phi_B = 0°$.

D (mm)	J (kg m^2)	B_p (N m s/rad)	K_p (N m/rad)	B_n (N m s/rad)	K_n (N m/rad)
4	3.6–12	1.1e−2	0.6	4.2e−3	0.3
5	9.8e−12	2.3e−2	1.4	9.8e−3	1.1
6	4.9e−11	7.2e−2	5.3	8.7e−2	2.5
8	7.1e−11	0.3	10.2	0.2	7.9
12	5.4e−10	0.7	87.0	1.1	74.0

3.1. *Model evaluation for flexible shaft*

The proposed torsional mass–spring–damper model in Eq. (10) is estimated from the straight to bending configuration of 90° using the input–output characteristics of flexible shafts at variable diameters and lengths. The model's coefficient values are estimated using the curve fitting toolbox of MATLAB for a white-box model using the Non-Linear Least Square method. The estimated physical parameters of inertia, stiffness, and damping for flexible shafts with variable diameter and fixed length are shown in Tables 1 to 5. Fig. 7 shows the measurements of the applied torque τ and the resulting twist angle θ along with the fitted model using Eq. (10). The section below discusses the evaluation in a straight and bending configuration for the cases of 0° to 45°, where the model performed quite accurately. For bending angle, $\phi_B = 45°$ onward, the model's goodness of fit deteriorates and is discussed by Fig. 10 in the section below.

3.1.1. *Straight configuration*

Fig. 7 shows the input–output characteristics for the selected set of flexible shafts along with the modeled version (10) for a straight configuration. The linear relationship between torque and twist angle θ implies that the stiffness term dominates in the model. In this case, the applied input could not excite the dynamics of a flexible shaft. The setup reaches its bandwidth limit due to its higher inertia than a flexible shaft. Thus, calculated inertia coefficients are used from Eq. (4). Table 1 shows the calculated parameters of inertia J and estimated parameters of stiffness (K_p, K_n) and damping coefficient (B_p, B_n) from the white box model (10). The model shows a good fit for all the flexible shafts with low percentage RMSE values with respect to the shaft's nominal torque for both positive and negative values of twist angle θ as shown in Table 2.

Observing the trend of model parameters in Table 1 for the increase in diameter is interesting. The inertia and stiffness values are directly associated with the geometry as given by Eqs. (4) and (8). The increase of coil-coil and coil-core stresses and friction on the flexible shaft's twisting can explain the damping coefficients trend.

The difference in values of physical parameters for the positive and negative sides of twist angle θ can be attributed to the winding and unwinding of the outermost coil layer. The values of inertia J are the same for both sides of twist angle θ due to no change in geometry. For the stiffness values, K_p and K_n differ due to the opposite direction of twist angle θ with respect to the direction of winding of the outermost layer as provided by the difference in Eqs. (8) and (9). For positive twist angle θ, the winding of the outermost layer winds onto the adjacent layer, making a tight, jam-packed, flexible shaft. However, for negative twist angle θ, the winding of the outermost layer unwinds, making it behave like a torsional spring, causing relief to the inner layers. As a result, the same flexible shaft portrays a slightly lower stiffness for K_n than K_p.

Table 2
RMSE values with respect to flexible shaft diameter — $\phi_B = 0°$ and 45°.

D (mm)	$pRMSE0_p$ (%)	$pRMSE0_n$ (%)	$pRMSE45_p$ (%)	$pRMSE45_n$ (%)
4	2	2	6	2
5	2	2	2	1
6	0.5	2	5.1	3.1
8	5.1	1.7	6	3.7
12	4	4	2.6	2.2

Table 3
Inertia torsional spring–damper model parameters — 15° bend angle.

D (mm)	J (kg m^2)	B_p (N m s/rad)	K_p (N m/rad)	B_n (N m s/rad)	K_n (N m/rad)
4	3.6−12	1.2e−2	0.5	8.5e−3	0.3
5	9.8e−12	2.8e−2	1.2	9.1e−3	0.9
6	4.9e−11	1.4e−1	4.4	5.0e−2	2.2
8	7.1e−11	3.3e−1	9.0	0.23	7.1
12	5.4e−10	0.7	86.2	1.4	74.2

Table 4
Inertia torsional spring–damper model parameters — 30° bend angle.

D (mm)	J (kg m^2)	B_p (N m s/rad)	K_p (N m/rad)	B_n (N m s/rad)	K_n (N m/rad)
4	3.6−12	2.1e−2	0.3	1.2e−2	0.2
5	9.8e−12	8.2e−2	0.98	5.3e−2	0.72
6	4.9e−11	2.2e−1	3.2	6.3e−2	1.9
8	7.1e−11	4.2e−1	7.0	2.7e−1	6.2
12	5.4e−10	1.736	84.2	1.47	75.95

Table 5
Inertia torsional spring–damper model parameters — $\phi_B = 45°$.

D (mm)	J (kg m^2)	B_p (N m s/rad)	K_p (N m/rad)	B_n (N m s/rad)	K_n (N m/rad)
4	3.6−12	1.9e−2	0.31	1.1e−2	0.25
5	9.8e−12	6.6e−2	1.02	3.9e−2	0.7506
6	4.9e−11	2.3e−1	2.5	6.7e−2	1.7
8	7.1e−11	4.0e−1	4.8	2.7e−1	4.82
12	5.4e−10	1.9	74.63	1.9	72.4

The values of B_p and B_n differ due to the less viscous nature of the flexible shaft on the winding of the outermost coil layer than its unwinding. The unwounded outermost layer offers more damping than the tightly wounded one. There is an increase in damping coefficients for both the positive and negative twist angle with the increase in diameter, as shown in Table 1. This highlights and validates the hysteresis increase with the increase in diameter discussed in the previous section.

Table 2 shows the percentage $RMSE_p$ and $RMSE_n$ values of the peak torque applied in measurements for the positive and negative side of twist angle θ with respect to the diameter of flexible shafts. The low percentage values show that the model fits all the variable diameter flexible shafts.

3.1.2. Bending configuration

Fig. 7 shows the input–output characteristics for the set of flexible shafts along with the simulated model (10) for the bending case of 45°. Table 5 shows the calculated parameters of inertia J from (4) and estimated parameters of stiffness (K_p, K_n) and damping coefficient (B_p, B_n) for the bending angle, $\phi_B = 45°$. The percentage RMSE values of peak applied torque for bending configuration of 45° at both positive and negative values of twist angle θ are shown in Table 2.

Fig. 10 and Tables 3 to 5 show the behavior of change of input–output characteristics over the increase in bend and diameter of the flexible shafts. The values of stiffness K_p and K_n for respective positive and negative twist angle θ, decline with the increase of bending angle, ϕ_B from 15° to 45°. With the increase in bend, the torsional stiffness of flexible shafts reduces with the increased bending stresses. The decline in torsional stiffness results in lowering the helical buckling limit. This means more stress due to helical buckling in combination with bending stress.

Fig. 7 depicts the increase in hysteresis with the increase in diameter. This trend results in a deteriorating fit of the simulated model in Fig. 7. Due to the increase in the diameter of coils and their wires, there is more friction due to the stresses of adjacent coil layers of the flexible shaft. Additionally, the hysteresis becomes dominant with the increased bending angle, ϕ_B of the flexible shaft. The increase in bending angle, ϕ_B makes it difficult to deliver torque over a bend for a flexible shaft. This causes a decrease in

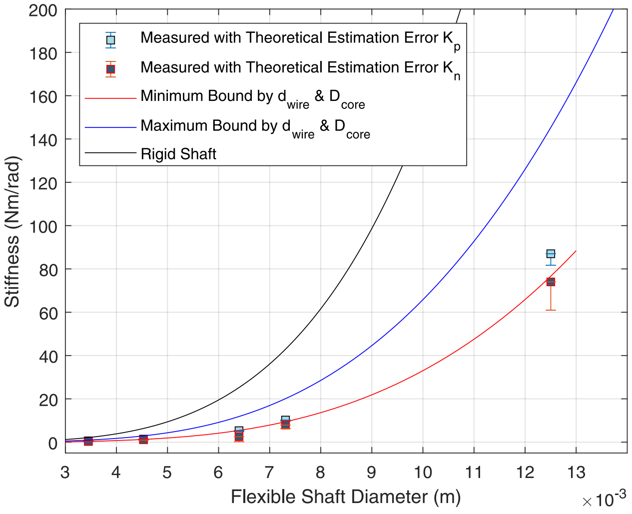

Fig. 12. Estimated stiffness K_p and K_n with theoretical error bound.

torsional stiffness and an increase in helical buckling. Consequently, the shaft undergoes more energy loss due to increased torsion, bending, and helical buckling deformations, as shown in Fig. 10.

At bending angles, ϕ_B more than 45°, the model deviates due to the highly non-linear behavior of flexible shaft as shown in Fig. 10. The prominent effect of helical buckling and bending makes the output torque relationship with the flexible shaft's twist angle highly non-linear. The proposed model focused on the flexible shaft's torsional deformation does not explain this behavior.

Table 2 shows the goodness of fit deteriorates for a bend configuration of 45° compared to the straight configuration 0° for the positive and negative values of twist angle, θ. The percentage RMSE values are calculated by dividing the RMSE values by the peak applied torque for each flexible shaft.

3.2. Evaluation of model-based physical parameters

Fig. 12 shows estimated stiffness values of a set of flexible shafts with fixed lengths and variable diameters obtained by parameter estimation for model (10) in Table 1. These estimated stiffness values are compared with the theoretical values obtained through the proposed geometric model by Eq. (8) using algorithm 1 in Section 1.3. The estimated values of stiffness K_p and K_n come from the values in Table 1 i.e., straight configuration for the positive and negative values of twist angle θ. To mark the possible construction of flexible shafts, the maximum and minimum bound plot for theoretical stiffness values is provided with a domain interval of possible core diameter, D_{core}, and the diameter of the coil's wire, d_{wire} as introduced in Section 1.3. Fig. 12 also shows the stiffness profile of rigid shaft using Eq. (3).

It can be observed that the theoretical estimation has more deviation from the estimated stiffness values with the increased diameter of the flexible shafts. This can be explained by the increased effect of the polar moment of inertia of the flexible shaft's core and its increased uncertainty. However, it is bounded by the minimum and maximum bound of the possible construction of flexible shafts. This is done in analogy to spring index C for the case of torsional spring to mark the region of possible stiffness values. The proposed estimation methodology by geometry offers more accurate results than Eq. (8) for a rigid shaft, as shown in Fig. 12. This validates the usability of geometry-based estimation of flexible shafts' stiffness. Thus, if a robotic system as in Fig. 1 requires a particular series stiffness with a specific link length, a flexible shaft of the corresponding diameter and length can be chosen using the geometric model (8).

Fig. 13 shows the trend of stiffness values of K_p and K_n with respect to change in length for the positive and negative twist angle θ. One can observe a nearly linear decline in stiffness with the change in length for both trends. The positive side of the twist angle shows a better fit with a line than the negative side. It is important to note that Eqs. (3) and (8) provide a linear relationship with the change in length, validating the effect of change in length on the stiffness of flexible shafts. The error box plots, as shown in Fig. 13, highlight the validation of model (8) and the usability of algorithm 1, though not so accurately due to the uncertainty of the diameter of core and wire diameters (see Fig. 14).

Another essential characteristic of flexible shafts is their change in torsional stiffness with respect to bending angle changes. For the case of fixed length and variable diameter flexible shafts, the bending experiments have shown nearly a linear decline in their stiffness with the increase in the bending angle, ϕ_B till 45°. However, after bending angles($\phi_B > 45°$), the decline in stiffness is non-linear. Fig. 10 shows the drop of the slope of torque-twist angle plots. This change in the stiffness values due to the bend of the flexible shaft cannot be explained by the model (8) and (10) due to its torsional characteristics only.

To incorporate the effect of bending on the stiffness of flexible shaft, an empirical formulation can be developed by using the stiffness values of nine flexible shafts at bending angles till 45° to form a 3D surface based on the values of length, L, D, and ϕ_B, as

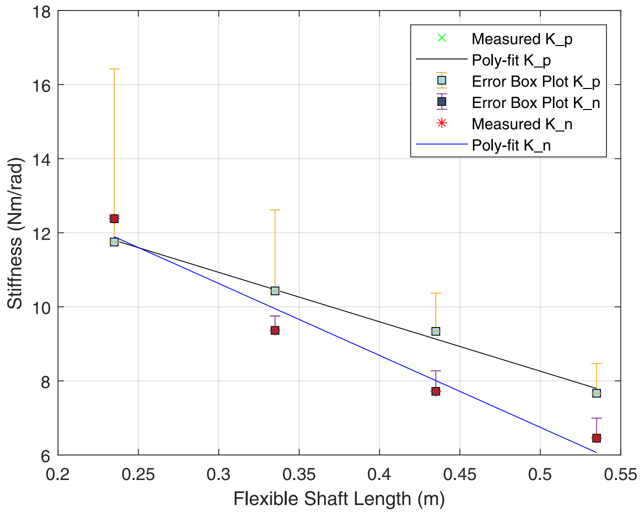

Fig. 13. Relationship of stiffness K_p and K_n with L.

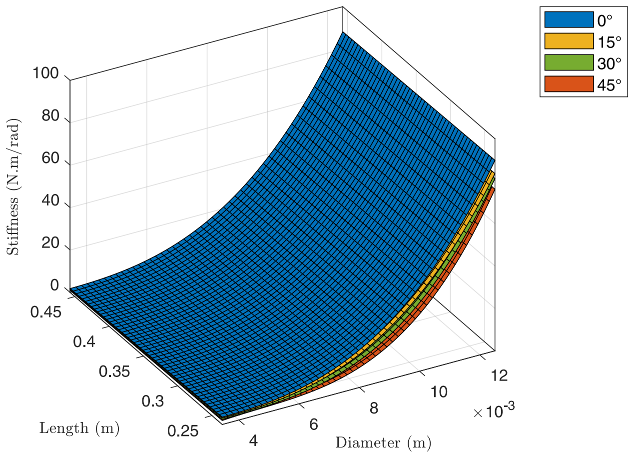

Fig. 14. Surface plots of stiffness K_p with D, L and ϕ_B.

Table 6
Coefficients of empirical formula for stiffness K_p and K_n as $f(D, L, \phi_B)$.

	$Coefficients_p$	$Coefficients_n$
p0	−1.8954	6.9716
p1	4.454e03	6.7431e02
p2	−1.102e06	−5.0267e05
p3	1.0693e08	7.3049e07
p4	−5.7768	−9.712
p5	−0.56092	0.83129
p6	−1.0166e+05	−1.0389e05

shown in Fig. 14. It can be utilized for estimating stiffness values at a particular bending angle for a flexible shaft with a particular diameter and length. The following equation gives the formulation obtained through interpolation and non-linear regression:

$$k(D, L, \theta) = p_0 + p_1 D + p_2 D^2 + p_3 D^3 + p_4 L + p_5 \theta + p_6 D^2.\theta \tag{11}$$

Table 6 provides the coefficient values for positive and negative sides of twist angle θ. This is performed to provide insight into the change of stiffness values with the change of bending angles. For a flexible shaft to be routed across a joint with a specific range of motion, the remotely actuated joint's stiffness variation can be studied using this formulation. Additionally, the extensive experimental study is put together in one formula to extract the stiffness values of the flexible shaft for the desired set of input values to develop a remote actuation module.

These coefficient values are estimated using non-linear regression on the stiffness values obtained through the model Eq. (10) using experimental results. An initial structure of the equation is assumed as per the relationships of diameter, length, and bending angle with the stiffness of a flexible shaft. The coefficients of the equation are estimated to achieve the best fit possible using MATLAB fit function. The rate of change of stiffness with respect to diameter and length is used to interpolate the data as a 3-D surface. This provides a space of points for the stiffness, diameter, and length values for a designer to pick and design an actuator based on a flexible shaft till the bending angle 45°.

4. Discussion

Using the proposed geometric method introduced in Section 1.3, the polar moment of inertia and stiffness of the flexible shafts can be better estimated than a rigid shaft's equation (2). Due to the uncertainty introduced by the assumption of the core's dimension in a flexible shaft in Section 1.3, there is a probable error in the coefficient values evident in Fig. 12. However, it can be bounded by minimum and maximum stiffness profiles using the possible construction values for the flexible shaft's core diameter, D_{core}, and wire's diameter, d_{wire}. Thus, the desired series stiffness and remote actuation are achievable using a flexible shaft by selecting corresponding diameter and length values using Eq. (8), though with a region of uncertainty due to different possible construction of flexible shafts. Similarly, in Fig. 13, one can observe a linear relationship of stiffness for K_p and K_n as provided by Eqs. (1) (3) [30]. In Fig. 13, the error is more dominant for K_p values than K_n due to the more number of layers considered for estimating the polar moment of inertia and stiffness, hence, susceptible to more uncertainty. The main reason behind the errors is also the probable error in the possible construction values of the flexible shaft's core diameter, D_{core}, and wire's diameter, d_{wire}. This resembles the uncertainty in values of the spring catalog, where there is an expected error of quoted and actual stiffness values.

Ideally, every shaft should be cut open to measure all the wires and core diameters to be exact in estimation. However, this results in the irreversible destruction of flexible shafts, which is non-economical. By not cutting open the flexible shaft, the model helps to estimate the torsional stiffness of a flexible shaft by only using manufacturers' given parameters or by simply doing external measurements of a flexible shaft to expedite the design process. The error is a price to pay to estimate the stiffness of a flexible shaft by measuring its parameters externally.

Flexible shafts are slender and long cables that offer very small inertia values. These values are insignificant for robotic applications with higher inertia as a load or a source compared to the inertia of a flexible shaft. However, a dominant effect of flexible shaft inertia can only be seen for applications involving high frequencies, low inertial power sources, and payloads. Thus, the experimental validation of the inertia of flexible shaft is not achieved directly but through the stiffness values as a function of the polar moment of inertia. Thus, the proposed inertial torsion spring–damper model encapsulates the range of applications by estimating a flexible shaft's polar moment inertia and stiffness parameters through geometry.

Knowing that stiffness is an essential characteristic of a flexible shaft for high torque and slow speed applications, the asymmetrical nature of flexible nature is studied separately. The model encapsulates both directions of rotation of a flexible shaft with a separate set of inertia, stiffness, and damping parameters for an inertial spring–damper model. A series of experiments are performed to characterize flexible shafts with a set of variable diameter and fixed length and a set of fixed diameter and variable length. The experimental results are modeled with a white box model of the inertial spring–damper model for both positive and negative sides of twist angle θ.

Damping and stiffness coefficient tends to increase with the diameter of the flexible shafts. However, the stiffness governs the input–output characteristics and explains the behavior of nearly constant stiffness for all nine flexible shafts with variable diameters and lengths. With the increase in bend, the hysteresis increases due to increasing deformation of the shafts in bending, torsion, and helical buckling. These coincident deformations introduce non-linearity for thin and long flexible shafts. The inertial spring–damper model based on torsional deformation cannot explain the behavior introduced due to the bending and helical buckling. This limits the model validity till 45° beyond which high non-linear torque versus twist angle characteristics are observed as shown in Fig. 10.

The increase in diameter increases the stiffness of a flexible shaft non-linearly, as shown in Fig. 12. In the case of length, the stiffness varies linearly in an inverse proportion. On bending the flexible shaft, the stiffness declines non-linearly with the increase in bending angle, ϕ_B. For smaller diameters, the change in stiffness value under the bending angle is observed to be changing very little for the increment of 15°. It can be observed for the diameter 4 and 5 mm flexible shaft, the change in stiffness value from 30 to 45° bending angle is non-existent or increased a bit above. The estimated stiffness using the mass spring–damper model also tends to be more inaccurate near 45° bending angle, creating more uncertainty in values. The stiffness behavior about length and diameter are explainable using Eqs. (8) and (9). However, the proposed model cannot explain bending behavior due to being focused on a 1-D deformation. An empirical non-linear regression formulation is provided using the experimental values of nine flexible shafts at different configurations. This formulation can facilitate the actuator design even with the change in stiffness due to bending. Nonetheless, for the complete characterization of flexible shafts, there is a need to understand three-dimensional elasticity and incorporate the torsion, bending, and helical buckling deformation together in a single model.

In this study, the focus has been mainly on modeling the characteristics of flexible shafts with the assumption that other robot parts are rigid. The parts comprising flexible shafts are assumed to be rigid and designed to allow the bending of flexible shafts along a single curvature with no interference. As it is evident in Fig. 9, the bend of the flexible shaft for high bending angles of 90° will become non-feasible and most likely interfere with the link components. Hence, a bend angle of 45° is proposed as feasible for the design, which aligns well with the model limitation. A bending moment is applied to the robot joint through which the flexible shaft passes to transmit torque to the distal joint. This is important for the robot's control perspective, where the bending stiffness of the flexible shaft can be used. Due to the 3-D nature of the deformation of the flexible shaft, a set of reaction forces and moments are experienced in the structure of the robot. The reaction forces and moments are important for the robot's structural design and require in-depth study using advanced models. For brevity, these studies are left in this work.

5. Conclusion and future work

A geometry-based polar moment of inertia and stiffness estimation method is proposed for flexible shafts and evaluated with experimental values in a straight configuration. Now, a user can estimate the stiffness of a flexible shaft without cutting it open by making measurements from its surface using the proposed model. An inertial spring–damper model based on the torsional stiffness of flexible shafts is proposed with scalability in its physical parameters of diameter and length by stiffness coefficients. The proposed model demonstrates its goodness of fit by low percentage RMSE values from the straight configuration of 0° to the bending configuration of 45°. For the bending angles, $\phi_B > 45°$, the model cannot explain the increased non-linearity due to the dominating effect of helical buckling and bending stresses. The paper provides insights into different characteristics of flexible shafts relating to geometry. An empirical model is proposed for incorporating bending angle and is feasible for robotic applications with a bend of up to 45°.

Although with its simplicity, a torsional mass–spring–damper model offers a simple explanation of the flexible shaft's behavior, it cannot explain the non-linear behavior for higher bending angles. In future work, the effect of helical buckling and bending deformation will be incorporated with torsional deformation to explain the behavior of flexible shafts at higher bending angles. Particularly, the inter-dependency of torsion and bending stiffness will be modeled using techniques involving the three-dimensional elasticity of slender rods. The limited nature of the torsional mass–spring–damper model will be further generalized for broader applicability in robotics applications using physics-based modeling. Modeling techniques like lumped parameters, finite elements, and the Cosserat theory of elastic rods will be compared to provide a real-time model of flexible shafts involving high deformations. From the robot's design perspective, the use and effect of conduits around flexible shafts to restrain helical buckling at bends will be studied. The influence of a flexible shaft on the robot's structure due to helical deformation will be investigated using Cosserat's Model. Furthermore, the bending moment applied to the preceding joint will be investigated to optimize the robot's design and control.

CRediT authorship contribution statement

Muhammad Usman: Writing – review & editing, Writing – original draft, Visualization, Validation, Software, Methodology, Investigation, Formal analysis, Data curation, Conceptualization. **Amin Khorasani:** Writing – review & editing. **Thierry Hubert:** Writing – review & editing. **Raphaël Furnémont:** Writing – review & editing, Supervision. **Bram Vanderborght:** Writing – review & editing, Supervision, Project administration, Funding acquisition. **Dirk Lefeber:** Writing – review & editing, Supervision, Funding acquisition. **Greet Van de Perre:** Writing – review & editing, Supervision, Funding acquisition. **Tom Verstraten:** Supervision, Project administration, Funding acquisition.

Declaration of competing interest

The authors declare that they have no known competing financial interests or personal relationships that could have appeared to influence the work reported in this paper.

Data availability

Data will be made available on request.

References

[1] G. Pratt, M. Williamson, Series elastic actuators, in: Proceedings 1995 IEEE/RSJ International Conference on Intelligent Robots and Systems, Vol. 1, Human Robot Interaction and Cooperative Robots, 1995, pp. 399–406, http://dx.doi.org/10.1109/IROS.1995.525827, vol. 1.

[2] D.W. Robinson, Design and Analysis of Series Elasticity in Closed-Loop Actuator Force Control (Ph.D. thesis), Massachusetts Institute of Technology, 2000.

[3] C. Lee, S. Kwak, J. Kwak, S. Oh, Generalization of series elastic actuator configurations and dynamic behavior comparison, Actuators 6 (2017).

[4] T. Verstraten, P. Beckerle, R. Furnémont, G. Mathijssen, B. Vanderborght, D. Lefeber, Series and parallel elastic actuation: Impact of natural dynamics on power and energy consumption, Mech. Mach. Theory 102 (2016) 232–246.

[5] T. Verstraten, J. Geeroms, G. Mathijssen, B. Convens, B. Vanderborght, D. Lefeber, Optimizing the power and energy consumption of powered prosthetic ankles with series and parallel elasticity, Mech. Mach. Theory 116 (2017) 419–432.

[6] W.T. Townsend, J.K. Salisbury, Mechanical design for whole-arm manipulation, in: P. Dario, G. Sandini, P. Aebischer (Eds.), Robots and Biological Systems: Towards a New Bionics?, Springer Berlin Heidelberg, Berlin, Heidelberg, 1993, pp. 153–164.

[7] H. Song, Y.-S. Kim, J. Yoon, S.-H. Yun, J. Seo, Y.-J. Kim, Development of low-inertia high-stiffness manipulator lims2 for high-speed manipulation of foldable objects, in: 2018 IEEE/RSJ International Conference on Intelligent Robots and Systems, IROS, 2018, pp. 4145–4151, http://dx.doi.org/10.1109/IROS.2018.8594005.

[8] S. Grosu, Laura De Rijke, V. Grosu, J. Geeroms, B. Vanderborght, D. Lefeber, C. Rodriguez Guerrero, Driving robotic exoskeletons using cable-based transmissions: A qualitative analysis and overview, ASME Appl. Mech. Rev. 70 (2018).

[9] J. Zhang, J. Zhang, Z. Kan, Z. Kan, Y. Li, Y. Li, Z. Wu, Z. Wu, J. Wu, J. Wu, H. Peng, H. Peng, Novel design of a cable-driven continuum robot with multiple motion patterns, IEEE Robot. Autom. Lett. (2022).

[10] N. Song, M. Zhang, F. Li, Z. Kan, J. Zhao, H. Peng, Dynamic research on winding and capturing of tensegrity flexible manipulator, Mech. Mach. Theory (2024).

[11] J.F. Veneman, R. Ekkelenkamp, R. Kruidhof, F.C. van der Helm, H. van der Kooij, A series elastic- and bowden-cable-based actuation system for use as torque actuator in exoskeleton-type robots, Int. J. Robot. Res. 25 (2006) 261–281.

[12] T. Lens, O. von Stryk, Investigation of safety in human–robot-interaction for a series elastic, tendon-driven robot arm, in: 2012 IEEE/RSJ International Conference on Intelligent Robots and Systems, 2012, pp. 4309–4314, http://dx.doi.org/10.1109/IROS.2012.6386236.

[13] S. Grosu, C. Rodriguez-Guerrero, V. Grosu, B. Vanderborght, D. Lefeber, Evaluation and analysis of push-pull cable actuation system used for powered orthoses, Front. Robot. AI 5 (2018).

[14] M. Quigley, A.T. Asbeck, A.Y. Ng, A low-cost compliant 7-dof robotic manipulator, in: IEEE International Conference on Robotics and Automation, 2011.

[15] H. Vallery, R. Ekkelenkamp, H. van der Kooij, M. Buss, Passive and accurate torque control of series elastic actuators, in: 2007 IEEE/RSJ International Conference on Intelligent Robots and Systems, 2007, pp. 3534–3538, http://dx.doi.org/10.1109/IROS.2007.4399172.

[16] G. Palli, G. Borghesan, C. Melchiorri, Tendon-based transmission systems for robotic devices: Models and control algorithms, in: 2009 IEEE International Conference on Robotics and Automation, 2009, pp. 4063–4068, http://dx.doi.org/10.1109/ROBOT.2009.5152491.

[17] Z. Liu, Z. Liu, Z. Cai, Z. Cai, H. Peng, H. Peng, X. Zhang, X. Zhang, Z. Wu, Z. Wu, Morphology and tension perception of cable-driven continuum robots, IEEE-ASME Trans. Mech. (2022).

[18] H. Peng, H. Yang, F. Li, C.M. Yang, N. Song, A unified framework for mechanical modeling and control of tensegrity robots, Mech. Mach. Theory (2024).

[19] D. Rodriguez-Cianca, C. Rodriguez-Guerrero, T. Verstraten, R. Jimenez-Fabian, B. Vanderborght, D. Lefeber, A flexible shaft-driven remote and torsionally compliant actuator (rtca) for wearable robots, Mechatronics 59 (2019) 178–188.

[20] A. Bicchi, G. Tonietti, Fast and soft-arm tactics [robot arm design], IEEE Robot. Autom. Mag. 11 (2004) 22–33.

[21] Y. Sekiguchi, Y. Kobayashi, Y. Tomono, H. Watanabe, K. Toyoda, K. Toyoda, K. Konishi, M. Tomikawa, M. Tomikawa, S. Ieiri, K. Tanoue, M. Hashizume, M.G. Fujie, Development of a Tool Manipulator Driven By a Flexible Shaft for Single Port Endoscopic Surgery, IEEE, 2010.

[22] N. Tan, X. Gu, H. Ren, Design, Characterization and applications of a novel soft actuator driven by flexible shafts, Mech. Mach. Theory (2018).

[23] R. Hayashi, K. Nicho, Y. Yu, T. Kinugasa, H. Amano, Small search robot consisting of plural driving wheels connected by flexible shafts, J. Robot. Mechatronics 26 (2014) 469–476.

[24] D. Kim, D. Lee, S. Joe, B.-I. Lee, K.-J. Cho, The flexible caterpillar based robotic colonoscope actuated by an external motor through a flexible shaft, J. Mech. Sci. Technol. 28 (2014).

[25] E. Tanaka, K. Muramatsu, K. Watanuki, S. Saegusa, L. Yuge, Walking assistance apparatus enabled for neuro-rehabilitation of patients and its effectiveness, Mech. Eng. Lett. 1 (2015) 15–00530–15–00530.

[26] Y. Hua, M.-Y. Xu, K. Osawa, E. Tanaka, Gait-adaptive method of an ankle-assist robot for walking promotion, in: The Proceedings of JSME Annual Conference on Robotics and Mechatronics, Robomec, 2023.

[27] H. Ooki, S. Yokota, A. Matumoto, D. Chugo, S. Muramatsu, H. Hashimoto, Development of walking assistance orthosis by inducing trunk rotation using leg movement: 1 st report on prototype and feasibility experiment, in: Proceedings of the 20th International Conference on Informatics in Control, Automation and Robotics - Volume 1, ICINCO, INSTICC, SciTePress, 2023, pp. 740–746, http://dx.doi.org/10.5220/0012235200003543.

[28] Q. Liu, X. Gu, N. Tan, H. Ren, Soft robotic gripper driven by flexible shafts for simultaneous grasping and in-hand cap manipulation, IEEE Trans. Autom. Sci. Eng. 18 (2021) 1134–1143.

[29] M. Kapitaniak, V.V. Hamaneh, M. Wiercigroch, Torsional vibrations of helically buckled drill-strings: experiments and fe modelling, J. Phys. Conf. Ser. (2016).

[30] A. Wahl, Mechanical Springs, McGraw-Hill, 1963.

[31] S. Kawamura, T. Yamamoto, D. Ishida, T. Ogata, Y. Nakayama, O. Tabata, S. Sugiyama, Development of passive elements with variable mechanical impedance for wearable robots, in: Proceedings 2002 IEEE International Conference on Robotics and Automation (Cat. No. 02CH37292), Vol. 1, 2002, pp. 248–253, http://dx.doi.org/10.1109/ROBOT.2002.1013369, vol. 1.

[32] K.J. Åström, R. Murray, Feedback Systems: An Introduction for Scientists and Engineers, Princeton University Press, 2021.

[33] K. Langlois, T. van der Hoeven, D. Rodriguez Cianca, T. Verstraten, T. Bacek, B. Convens, C. Rodriguez-Guerrero, V. Grosu, D. Lefeber, B. Vanderborght, Ethercat tutorial: An introduction for real-time hardware communication on windows [tutorial], IEEE Robot. Autom. Mag. 25 (2018) 22–122.